OCEAN APPLICATIONS TECHNICAL NOTE 15

Interannual and decadal variability in the tropical Pacific.

by

Simon F B Tett, Michael K Davey and Sarah Ineson

Met Office
FitzRoy Road, Exeter, Devon. EX1 3PB

Interannual and decadal variability in the tropical Pacific

Simon F. B. Tett, Michael K. Davey and Sarah Ineson
Hadley Centre, U.K. Met. Office,
London Rd, Bracknell,
Berks RG12 2SY
UK

Abstract

The interannual and decadal variability in observations and in related coupled general circulation models is analysed. The models have substantial interannual variability, but typically concentrated at shorter periods than observed. Variance and lag correlation maps are used to highlight several important interannual features. Observed equatorial features are simulated better when enhanced tropical ocean resolution is used. For decadal variability the long Southern Oscillation record provides a means of comparing models and observations.

1 Introduction

Differences in regional climate from one year to the next, such as seasonal rainfall variations, can have large direct and indirect effects on society. The largest such interannual variability occurs in the tropical Pacific, where strong ocean-atmosphere interaction associated with the warm seas generates substantial anomalies. These El Niño Southern Oscillation (ENSO) events have a global impact, and in many regions interannual climate anomalies are significantly associated with the cycle of these events. Glantz *et al* (1991) provide a wide-ranging review of ENSO and its impacts. Background information and an atlas of ENSO impacts since 1871 can be found in Allan *et al* (1996).

Understanding the ENSO phenomenon was a major goal of the Tropical Ocean Global Atmosphere (TOGA) programme. During TOGA (1985-1994), substantial advances were made through the use of enhanced observational

networks and the application of a range of models. (For reviews, see TOGA (1997).)

The most complex climate models consist of coupled atmosphere and ocean general circulation models (AOGCMs). However simple coupled models, using reduced physics atmospheres or statistical atmospheres coupled to shallow water type ocean models are quite successful in simulating and predicting the timing and magnitude of significant SST anomalies in the equatorial east Pacific (Zebiak and Cane, 1987; Barnston *et al*, 1994). It is hoped that the continuing development of fully coupled AOGCMs will eventually lead to better and more comprehensive predictions, including the impacts on the extra-tropics from changes in the position of the warm pool and associated convective centres.

As well as interannual changes, there are climate fluctuations on decadal and longer scales(Parker *et al*, 1994) with evidence of decadal variations in ENSO (Diaz and Markgraf, 1992; Balmaseda *et al*, 1995; Gu and Philander, 1995; Wang and Ropelewski, 1995; Wang, 1995), and of extratropical variations(Mann and Park, 1994; Kushnir, 1994). Such variations also involve ocean-atmosphere interaction, and coupled models have provided insight into some likely mechanisms (Latif, 1996; Latif and Barnett, 1994; Latif and Barnett, 1996; Delworth, 1996; Chang *et al*, 1997).

On interdecadal timescales, AOGCMs are used to make predictions about changes in the climate of the Earth as greenhouse gases such as CO_2 increase. Several modelling centres have made long integrations using coupled models to examine the transient effects of increases in such gases (Washington and Meehl, 1989; Manabe *et al*, 1991; Murphy and Mitchell, 1995). More recently experiments have been run with such models in an attempt to simulate past climate change(Mitchell *et al*, 1995). Recent work in the detection of anthropogenicaly caused climate change relies on model estimates of natural variability on interdecadal and greater timescales (e.g. Santer *et al* (1996); Tett *et al* (1996)). Confidence in the results of these coupled models can be increased if the processes such as ENSO occurring in the observed coupled system are properly reproduced by these models.

This chapter contains examples of the analysis and assessment of interannual and decadal variability in three AOGCMs which have been developed at the Hadley Centre, United Kingdom Meteorological Office (UKMO). The models, referred to as HADCM, HADCM2 and TOGAGCM, are described in section 3 while the datasets used to compare the models and observations are described in section 2. HADCM and TOGAGCM use the same AGCM, but have different ocean components (global and regional Pacific respectively).

In section 4, the interannual tropical Pacific behaviour of HADCM and TOGAGCM is described and compared with observed behaviour, concentrat-

ing on sea surface temperature (SST) and upper ocean vertically averaged temperature (VAT) fields.

In section 5, brief examples of results from a 1200 year integration of a more recent AOGCM developed at the Hadley Centre, HADCM2, are described.

2 Data sources

In the study reported in this chapter we use several datasets:

1. The Earth Radiation Budget Experiment (ERBE) (Harrisson *et al*, 1990) data provides observed top of the atmosphere outgoing longwave radiation (OLR) and shortwave albedo for the 1985–89 period. In the tropics OLR is a good proxy for convective activity (Zhang, 1993). In regions of high OLR the shortwave albedo gives an indication that low cloud is present.

2. For SST, we used the UKMO monthly Global Ice and Sea Surface Temperature (GISST) dataset (Parker *et al*, 1993), which is a development of a previous UKMO global sea surface temperature data-set described in the atlas by Bottomley *et al* (1990). We use the period 1962 to 1993 from this data-set.

3. A Pacific Ocean analysis (assimilating ocean surface and sub-surface temperature observations into an OGCM (Leetmaa and Ji, 1989)) from the US National Meteorological Center was used to provide an estimated ocean temperature dataset from the surface to a depth of 360.0 metres. The so-called RA3 dataset (Ji *et al*, 1995; Smith and Chelliah, 1995; Ji and Smith, 1995) for the 126 month period from July of 1982 to December of 1992 was used.

4. The final dataset we use is a long term record of the Southern Oscillation Index (SOI) (Parker, 1983) covering the period from 1866 to 1991.

3 Model Description

In this section we provide some details of the the three related AOGCMs (HADCM, HADCM2 and TOGAGCM).

The global AGCM used in all the coupled integrations described below has resolution of 2.5° latitude by 3.75° longitude with 19 levels on a hybrid

co-ordinate vertical grid. A split-implicit integration scheme is used allowing a timestep of 30 minutes. A comprehensive physics package is used, including a stability dependent cloudy boundary layer scheme (Smith, 1990), a land surface hydrology scheme (Gregory and Smith, 1990; Dolman and Gregory, 1992) and a radiation scheme with interactive optical properties (Slingo, 1989). The mass flux convection scheme used to represent shallow, deep and mid-level convection (Gregory and Rowntree, 1990) has been modified by the inclusion of deep convective downdraughts. A more comprehensive overview of the atmospheric model can be found in Cullen (1993).

The OGCMs are variations of the basic Bryan/Cox finite difference model (Cox, 1984). A mixed layer model, based on that of Kraus and Turner (1967), is embedded in the ocean models and the K-theory mixing scheme of Pacanowski and Philander (1981) is used to parameterize vertical turbulent mixing.

For HADCM and HADCM2 the ocean has 20 vertical levels, with 7 levels covering the top 113 metres. The depths and thicknesses of these levels are shown in table 1. For HADCM and HADCM2 the horizontal OGCM resolution of 2.5° latitude by 3.75° longitude, matching the AGCM horizontal resolution is relatively coarse to allow long integrations.

The HADCM2 AOGCM is a later development of the HADCM AOGCM. The major differences between the two include the treatment of ice, fixing an error in the location of the stress due to gravity wave breaking and correcting the Levitus salinities near Antarctica for summer bias used to derie the flux corrections. Further description of HADCM2 and its applications can be found in Johns *et al* (1997), Tett *et al* (1996); Mitchell *et al* (1995); Hewitt and Mitchell (1996) including a 1200 year integration in which forcing was kept constant. We analyse timeseries of tropical Pacific temperature and Southern Oscillation from this simulation.

The ocean model for TOGAGCM is limited to the tropical Pacific region between 30°N and 30°S, but has higher and variable horizontal resolution to represent equatorial processes more accurately. The horizontal grid has a meridional grid spacing of 1/3° at the equator, increasing to 1° at the northern and southern boundaries, and zonal grid spacing of 1.5° decreasing to 0.5° near the eastern and western boundaries. The vertical grid uses the upper 16 levels shown in table 1. The barotropic mode is omitted and there is no variation in model bottom topography. Temperature and salinity at open northern and southern boundaries are kept close to their seasonally varying climatological values by Haney forcing to Levitus (1982) values. Outside the ocean model domain, SST is kept fixed to the observed climatological seasonal cycle. The seasonal cycle of TOGAGCM model is described in Mechoso *et al* (1995), and further details of its interannual behaviour can be found in

Ineson and Davey (1997). The results discussed here are based on a 25 year integration of this model.

In each case the ocean models are coupled to the atmosphere model by the same procedure: heat and fresh water fluxes and windstress are accumulated by the atmospheric model and passed to the ocean every day. In the ocean model daily average values of SST are computed and passed to the atmosphere model once a day.

Flux adjustment is used in HADCM and HADCM2 to control climate drift. There is no flux adjustment in TOGAGCM, but the SST is constrained to observed climatology outside the ocean model domain.

Table 1: Ocean model level depths (m)

Model Layer	Thickness	Depth of mid-point
1	10.0	5.0
2	10.0	15.0
3	10.0	25.0
4	10.2	35.1
5	15.3	47.9
6	23.0	67.0
7	34.5	95.8
8	51.8	138.9
9	77.8	203.7
10	116.8	301.0
11	175.3	447.1
12	263.2	665.3
13	395.3	995.6
14	616.0	1501.1
15	615.0	2116.0
16	615.0	2731.0
17	615.0	3347.0
18	616.0	3962.0
19	615.0	4577.0
20	615.0	5193.0

4 Climatology and Interannual Variability

In this section the behaviour of HADCM and TOGAGCM in integrations of 20 and 25 years respectively is compared with observed behaviour, to

illustrate assessments of their skill at reproducing tropical climatology and variability.

4.1 Climatology

The observations show three convective centres (Fig. 1 (a) and (b)) whose positions change throughout the seasonal cycle: one centred over Indonesia which extends west into the Indian ocean and east into the west Pacific, another centred over Africa and the third over central America/South America. As noted by Meehl (1987) the movement throughout the seasonal cycle is a north to south and a west to east movement. Other important features are the warm SST pool in the west Pacific(Fig. 1 (a) and (b)), with temperatures greater than 29°C, and the region of cooler waters in the equatorial east Pacific. The feature of note in the cross section of near-surface ocean temperature is the strong thermocline(Fig. 1 (c)), shallowest in the east Pacific and deepest in the west Pacific.

The SST pattern in HADCM (Fig. 2 (a) and (b)) is similar to that observed, with the model qualitatively capturing the large-scale features of the tropical SST in both July and January. There are several differences: during July the model warm pool is smaller than observed and mainly consists of a tongue of warm water (greater than 29°C) extending to the east of New Guinea with small regions of warm water near the Philippines. Compare this to the observations for July which show a large region of warm waters to the east of the Philippines. In the Indian ocean the waters around India are cooler than observed during July and January.

If we examine the regions of low OLR(Fig. 2 (a) and (b)), corresponding to regions of high convective activity, we find that the low OLR values associated with the Indian monsoon have too small an extent and the convection over the north west equatorial Pacific is too strong. During January HADCM suppresses convection in the Indonesian region and strengthens it over both the Indian and west Pacific Oceans. The model is generating convection over the Andes mountains; something not observed in nature. The other convective centres, over Africa and South America are smaller than the comparable centres in the observations. These errors in the placement of low OLR values are similar to those of an AMIP integration (not shown) strongly suggesting that the errors are due to problems in the atmospheric component of the model.

HADCM captures the major upper ocean features(Fig. 2(c)); the isotherms can be seen rising across the Pacific as we travel from west to east. In the East Pacific the thermocline is strong, but in the west and Central Pacific the thermocline is more diffuse than observed. Furthermore in the east Pa-

cific temperatures the subsurface temperatures below the thermocline are too warm, probably due to the excessive diffusion of heat through the model thermocline.

The equivalent plots for TOGAGCM are shown in Fig. 3. Only the SSTs from the active Pacific ocean model region are shown. In the west Pacific the model warm pool is cooler than the observed warm pool, with only very small regions where the temperature is greater than 29°C. The warm water in the west Pacific stretches too far to the the east. Furthermore the model is failing to capture the cold pool in the east Pacific. During January TOGAGCM generates a closed region of cooler waters near the equator. The TOGAGCM Pacific zonal temperature gradient is weaker than observed.

Like HADCM, the simulated subsurface temperatures in the east Pacific are too warm. The most likely explanation for this behaviour is that the surface waters are too warm in this region and more heat is diffusing down through the thermocline into the cooler waters below.

4.2 Inter-annual variance

The simulation of the observed tropical inter-annual variability by coupled GCMs is of considerable interest both for use in seasonal forecasting and for improving models used for climate prediction. Many modelling groups have described the ENSO-like behaviour of their coupled AOGCMs (Philander *et al*, 1989; Lau *et al*, 1992; Meehl, 1990; Nagai *et al*, 1992; Neelin *et al*, 1992; Philander *et al*, 1992; Sperber and Hameed, 1991; Tett, 1995; Robertson *et al*, 1995; Latif *et al*, 1993b; Latif *et al*, 1993a; Terray *et al*, 1995).

There are several different mechanisms causing ENSO like behaviour in different coupled models. The two principal modes which occur are a propagating (normally westwards) coupled SST mode, and another in which SST variability is controlled by eastward propagating changes in the thermocline depth with atmosphere/ocean feedbacks acting to amplify the SST anomalies. The second mechanism is believed to be responsible for the observed ENSO phenomenon (Philander, 1990). In most low resolution models the coupled SST mode is the primary mechanism for SST variability; however some models (Tett, 1995) have both mechanisms active.

In Neelin *et al* (1992) many coupled models were intercompared, primarily using time-longitude plots of equatorial SST anomalies. These figures can be difficult to interpret, in particular determining dominant frequencies and regions of maximum variability is difficult. These time-longitude diagrams only present data from the near equatorial region and do not encourage a statistical comparison, focusing attention on the detailed time behaviour of the individual models. In this subsection we carry out an intercomparison

by first examining total power in different frequency bands. This techniques focuses attention on the statistical properties of the model variance. We also compare timeseries of NINO3 SST to verify the usefulness of the technique.

In order to successfully intercompare models we need a method of characterizing their inter-annual variability in as compact a manner as possible. There are two characteristics of variability that we consider important; magnitude and dominant frequencies. We define inter-annual variance as the total power of a timeseries for all periods strictly greater than 12 months. This definition requires that the data be Fourier transformed and is different from the definitions used in other studies. Meehl *et al* (1994) define inter-annual variability in a different way; they define inter-annual variance as the variance of a 12 month running mean timeseries of monthly anomalies. A disadvantage of using a 12 month running mean is that it has effects on frequencies greater than 1 year. Furthermore in our method no removal of the seasonal cycle is required.

The observed major timescales of ENSO are the biennial timescale (Meehl, 1993; Rasmusson *et al.* 1990) and the 3 to 6 year timescale (Rasmusson and Carpenter, 1982). The way we propose to capture this behaviour is to examine the total power in two different period ranges; the 1+ to 3 year band and the 3+ to 6 year band. (By the 1+ to 3 year period range we mean the total power in all periods strictly greater than 1 year and less than or equal to 3 years.) The total power in a frequency range is the same as the variance of the timeseries which has been band-passed filtered in such a way that frequencies in the period range are unaffected while frequencies outside the range are completely removed. Examining maps of total power in these period ranges enables us to determine the major characteristics of the model interannual variability. We consider SST and the upper ocean vertically averaged temperature (VAT) from the models and observations. The first of these quantities is the primary means by which the ocean drives the atmosphere and the latter is a diagnostic for changes in thermocline depth. In the near equatorial Pacific changes in thermocline depth are associated with wind driven travelling Rossby and Kelvin waves.

Fig. 4 shows plots of total power in the two frequency ranges for the observed SST data-set and for the models. In the observed plots the largest values of total power occur in the equatorial eastern Pacific. The plots (Fig. 4(a) and (b)) of the two period ranges are very similar but there is slightly more power in the 3+ to 6 year period band. Compare that with the models; almost all the power is in the 1+ to 3 year range with relatively little power in the 3+ to 6 year band. Also apparent, especially in TOGAGCM, is that the models show a much narrower latitudinal extent of the equatorial variance maximum than do the observations.

HADCM has a SST power maxima at approximately 165°W peaking at a value of $0.3°C^2$. There is a long tail to the west of this stretching all the way to South America. The peak value ($0.4°C^2$) for this model is comparable to the observed 1+ to 3 year total power but the position is too far to the west.

TOGAGCM shows maximum values along the equator, with a large longitudinal extent and peak values ($> 0.8°C^2$) that are larger than those observed, at least in the 1+ to 3 year range.

To summarize, both models produce substantial SST variability in the tropical Pacific. However the power is largely in the the 1+ to 3 year frequency band with very small power in the 3+ to 6 year band. The observations show approximately equal amounts of variance in each band. The models do not reproduce the large variances in the eastern Pacific, tending instead to generate maxima in the central Pacific.

The results for VAT are similar, in that the models have very little power in the 3+ to 6 year range, so we focus on the the 1+ to 3 year VAT band. Fig. 5 shows plots of the inter-annual variance (total power for all periods greater than 1 year) in VAT from the surface to 360 metres from the NMC RA3 analysis and of total power in the 1+ to 3 year range for the two models. Recall that the observations are for only a 11 year period. The analysis shows clear evidence of large variability in the equatorial wave guide with an equatorial maximum in the east Pacific. There is also high variability spreading polewards along the coast of the Americas; this is consistent with poleward propagation of coastally trapped Kelvin waves. In the west Pacific maxima occur either side of the equator: at 8°S and, less distinctly, north of the equator at 10°N.

Both models also have variability peaks along the equator, suggesting that Kelvin waves are being excited by changes in zonal wind stress. However the total power in VAT is approximately four times weaker than that observed. (Like model SST, model VAT variance is even weaker beyond the 1+ to 3 year period range.)

HADCM seems to be generating VAT variability in the central wave guide region, but the total power seems to decline rapidly east of 140°W, suggesting that the model Kelvin waves are being rapidly damped as they propagate to the east. By contrast, in TOGAGCM we can see a clear signal of a variance maxima along the the equator. Further, the variance region expands polewards in the east Pacific suggesting that poleward propagation of coastal Kelvin waves is being reproduced. (Recall that TOGAGCM has enhanced resolution near the coasts as well as along the equator.) By contrast with the NMC analysis, TOGAGCM has a smaller meridional extent of the total power maxima.

In the west Pacific, HADCM has a substantial VAT variance peak north

of the equator only, at about 12°N, while TOGAGCM has a strong zonally extensive peak at 5°S and a weaker peak along 4°N. The off-equatorial west Pacific peaks in the models and observations are consistent with the idea that the wind stress variance is forcing westward traveling Rossby waves in this region.

4.3 Timeseries Analysis

In order to provide some verification of the filtered variance technique we shall now examine timeseries and their power spectra from the regions of maximum SST variance in the observations and in the models. As we have already shown, the regions of maximum variability in the models and observations are in different regions. In each case we have calculated area averages from 5°N to 5°S with a longitudinal extent of 15° centred on a region corresponding to the location of maximum variability. (105°W-90°W for observations, 165°W-150°W for HADCM, 150°W-135°W for TOGAGCM.) Fig. 6 shows plots of the area averaged monthly anomalies from the last 30 years of the GISST data-set and from the entire period of integrations for each model. The anomalies were computed by removing the mean annual cycle for the period that is shown.

It is clear from the modeled timeseries that the AOGCMs have a strong biennial mode, with strong warm events being followed by strong cold events. HADCM has peak to peak SST values of about 3 K, compared to the observations which have peak to peak values of about 5 K. HADCM2 also shows peak to peak SST variability of about 3K (Tett *et al*, 1997). TOGAGCM peak to peak SST variability is about 4 K, closer to the observed values. Recall that TOGAGCM shows a very narrow region of high variance and that the area-averaged timeseries covers a broader region. Also apparent in the modelled timeseries are quiescent and active oscillation regimes. For example, in TOGAGCM years 8 to 14 are active while for years 14 to 22 the model is quiescent. HADCM also shows similar behaviour but the distinction between active and quiet periods is less clear. This is in contrast to the observations which do not show such long periods of quiescence, at least since 1948.

Having computed these timeseries we then computed power spectra(Fig. 7). See Tett *et al* (1997) for details of these computations and the procedure followed to give the best-fit to an AR1 model.

Apparent in the observed power spectra (7(a)) are two significant but broad peaks; one centred on approximately 48 months and the other on the biennial period. Compare this with the AOGCMs, which have peaks only near the biennial period. In TOGAGCM the strength of this peak is

comparable with the maximum peak in the observed data-set. In general the power spectra confirm the picture that we drew earlier when we examined the total power in different period ranges.

4.4 SST and VAT propagation characteristics

So far we have not considered the direction and speed in which SST and VAT anomalies propagate: looking at total power does not enable us to do this. We now examine the propagation properties by computing lagged correlation of SST and VAT across the entire equatorial Pacific with the regions of maximum variability which we considered above. In particular by examining the characteristics of the maximum correlation of VAT with the SST we should be able to diagnose the mean wave speed in the wave guide. Furthermore by doing this we see if there any links between changes in VAT and changes in SST.

We carry out the computations by first taking monthly mean data from the equatorial Pacific Ocean and removing the mean seasonal cycle. Having done this we area average this data between 5°N and 5°S and removed high frequency noise by using a 1-2-1 time smoother. This process is carried out for both HADCM and TOGAGCM, and for the observations. For each one of these data-sets we then compute the correlation at all points and for all lags between -18 and $+18$ months, with the timeseries of SST from the region of greatest SST variability from the same model.

In the observations(Fig. 8), using data for 1962 to 1992, SST anomalies tend to move rapidly to the west from the eastern Pacific. They take approximately 2 months to reach the dateline where they decay. By contrast the coupled models show quite different behaviors. HADCM shows a standing pattern confined to the central Pacific with some evidence of eastward propagation occuring in the eastern Pacific, as does HADCM2 on the seasonal timescale(Tett *et al*, 1997). There is also a secondary region of large correlations occurring in the east Pacific with a lag of 2 months. TOGAGCM clearly shows a slow eastward propagation in the west Pacific and a significantly faster, but still eastward, propagation in the central and east Pacific. Clearly apparent in the correlation plot from TOGAGCM is a biennial signal. Also evident in the observational and AOGCM results is a region of negative correlations in the western Pacific at slight positive lags. In the two models this feature propagates slowly to the east until it reaches the dateline when it accelerates but still traveling eastward.

Having considered the propagation characteristics of SST anomalies we now use the same technique to examine VAT. Again we look at correlations with the regions of maximum SST variance (Fig. 9). Clearly apparent in the

observations(Fig. 9(a)) is a eastward traveling signal with maximum correlations at a lag of -1 month to the SST timeseries averaged over the region of maximum variance. Also clearly apparent is a triggering of negative anomalies at 150°E. The models(Fig. 9 (b) and (c)) also show clear evidence of eastward traveling signals. In both HADCM and TOGAGCM simulations negative VAT anomalies[1] are clearly apparent in the west Pacific at the same time that the positive VAT anomalies reach the east Pacific.

The speed of propagation changes between models and can be quite different in different places in the same data-set. We estimate the wave speed by examining the slope of maximum correlation and measuring the time lag between maximum correlation at 150°W, where all data-sets show correlations greater than 0.5, and at the coast of South America. This is a distance of 7.78×10^6m and a free Kelvin wave, traveling at 2.8m/sec would take approximately one month to travel this distance. The estimates that we make are only accurate to the nearest month as they are based on monthly mean data. Examining the observations we estimate that a signal takes approximately 3 months to travel this distance. In TOGAGCM and HADCM the VAT signal also takes about 3 months to travel the same distance.

In the west and Central Pacific analyzed VAT anomalies are moving much slower than in TOGAGCM. Maximum correlations in the west Pacific at 150°E lag those in the far eastern Pacific by 11 months in TOGAGCM and by 17 months in the observations. Some caveats are required when interpreting the NMC analysis data; it is only a 11 year dataset and the results are likely to be dominated by the strong event of 1982/3.

5 Decadal variability in ENSO

Observations that are of sufficient length to examine interdecadal variability in ENSO are quite sparse. The best long instrumental records available are surface Pressure measurements: the Southern Oscillation Index (SOI) provides a measure of large scale tropical pressure changes (see Allan *et al* (1996) for a review of SOI history and data). Reliable records of SST and winds also extend back to the last century, but early observations are sparse in space and time. (e.g. the Comprehensive Ocean Atmosphere DataSet, Woodruff *et al* (1987)) Proxy data such as tree rings and coral growth provide evidence on multi-century timescales; see articles in Diaz and Markgraf (1992).

Recent analysis of such observations ((Ropelewski and Jones, 1987; Parker *et al*, 1994; Mann and Park, 1994; Wang and Ropelewski, 1995; Gu and Philander, 1995) has suggested substantial ENSO variability on decadal scales.

[1] i.e. opposite sign to the SST anomalies.

There has been a relative maximum in El Niño activity toward the end of the 19th century, a minimum from late '20s to '50s, and relatively large variability to present. There is some evidence suggesting that ENSO variability is higher (lower) when climate mean SST is warmer (colder). Details are sensitive to the choice of SST dataset however.

The mechanism for decadal ENSO variations is not clear. Gu and Philander (1997) have proposed a mechanism involving subduction of water mass anomalies in the sub-tropical Pacific that are advected to the equatorial subsurface region and consequently influence SST variability and associated extratropical connections.

There are several ways of examining interdecadal behaviour, using various forms of time series analysis (simple spectra, filters, wavelets, singular spectra, etc.). When sufficient data is available (as is usually the case in model climate simulations) associated spatial structures can be extracted. Space does not allow a detailed analysis here: we shall simply provide some basic spectral examples.

We first compare the power spectrum of the observed SOI (based on Tahiti and Darwin surface pressure anomalies) with that simulated by the HADCM2 model (Fig. 10, (a) and (b)). The model SOI is defined in terms of rectangular regions around Darwin (125°W, 15°S – 130°W, 10S°S) and Tahiti (150°E, 20°S – 155°E, 15°S) that represent the centres of action: 1300 years of annual-mean model data are used. Best-fit red noise power spectra are indicated by the dash-dot curves, with dashed lines indicating corresponding 99 and 95% confidence limits.

The most distinct significant peak in the observed spectrum (Fig. 10b) occurs at about 7 years, with a weak, non-significant spectral peak at approximately 4 years. The HADCM2 SOI spectrum (Fig. 10a) has a well defined highly significant peak at approximately 8 years and a broad peak around 3 to 4 years. Qualitatively the observed and model spectra are similar. The absence of peaks at longer periods in the observations and model is striking. For periods from 10 to 200 years the simulated SOI shows no significant departures from white noise. Note that the simulated power is significantly greater than the observed power. HADCM2 overestimates interannual variability in the atmosphere, indicating that the AGCM probably reacts too strongly to SST anomalies.

The power spectrum of HADCM2 surface temperature variability in the central equatorial Pacific (Fig. 10c), also has a broad peak at 3-4 years and another peak at approximately 8 years. Generally, the model SST spectrum is quite similar to the SOI spectrum, which indicates strong ocean-atmosphere coupling on interannual scales. The similarity is less pronounced for observed SST and SOI spectra.

According to this limited analysis, HADCM2 (with relatively coarse ocean resolution) is capable of producing low frequency ENSO variability similar to that observed.

6 Summary

Examples of the analysis and comparison of observed and model low frequency variability have been presented. In this chapter we have concentrated mainly on oceanic features, but the same methods can be applied to atmospheric variables as well. In particular, the links between surface wind stresses and SST and VAT forcing and responses can be examined usefully in this way, as can the connections between the tropics and subtropics/extratropics. See Tett *et al* (1997) for some more examples.

The interannual variability was first assessed by comparing maps of variance in different period ranges. The AOGCM evidence presented here demonstrates (as found in other AOGCMs) that such models are able to produce significant interannual variability, but they differ in detail from observed behaviour and from each other.

For SST, the variance maps (Fig. 4) demonstrate that the models tend to concentrate interannual variability in the central equatorial Pacific, unlike the east Pacific maxima found in observations. With higher equatorial ocean resolution (TOGAGCM) the variability extends more strongly into the east Pacific, probably due to the better representation of equatorial Kelvin waves. Such waves are heavily damped when ocean resolution is relatively coarse as in HADCM and HADCM2. TOGAGCM also produced a more realistic spatial distribution of upper ocean variability (Fig. 5). The models have relatively little variability at periods longer than 3 years, again in contrast to the observations that have similar variability in the 1+ to 3 year and 3+ to 6 year bands. This disparity was confirmed by SST time series spectra (Fig. 7).

A feature of the analysis in this chapter is the use of lag correlations to compare and contrast the observations and models. Mapd of equatorial lag correlations provide information about speed and direction of movement that is often difficult to see directly in Hovmoller diagrams. Lag correlations of SST anomalies with SST in the region of maximum variance were calculated (Fig. 8). For observed SST, the result was a predominantly standing pattern, with the west Pacific out of phase with the central and east Pacific. The signal at zero lag was preceded (followed) by a signal of opposite sign with a lead (lag) of about 18 months. The AOGCM patterns were broadly similar, but with more signs of westward propagation (particularly in TOGAGCM,

which displayed a strong link from the west to central Pacific regions), and shorter lags for sign reversal.

Similar maps of lags between VAT and SST (Fig. 9) revealed strong eastward propagation in the observations (i.e. west (central) Pacific VAT changes preceded central (east) Pacific changes). This suggests that eastward movement of thermocline depth anomalies (which are strongly related to VAT changes) is the mechanism for the generation of SST anomalies that subsequently trigger positive feedbacks with the atmosphere. The eastward propagation evident in the observed SST/VAT relations was captured reasonably well by the OAGCMs. This picture agrees with that produced by more complicated principal oscillation pattern analysis, as in Latif *et al* (1993a); Davey *et al* (1994).

A multi-century run of HADCM2 was used to illustrate the analysis of decadal scale behaviour. Similar spectral peaks in the observed and simulated SOI spectra were noted (Fig. 10). There are significant (relative to best-fit red noise) peaks near a seven year period, but no significant peaks at longer periods. There may be predictability associated with the seven year peak.

The model SST spectrum revealed similar behaviour, with interannual ENSO peaks and a significant seven year peak, which suggests that the low frequency behaviour involves close ocean-atmosphere coupling.

The low frequency ENSO variations may be due to slow changes in the background state of the equatorial Pacific. This aspect has not been considered here, but merits attention due to its implications for practical prediction of ENSO and its impacts.

Bibliography

Allan, R. J., J. Lindesay, and D. Parker, 1996: El Niño Southern Oscillation and climatic variability. Technical report, CSIRO. 416pp.

Balmaseda, M., M. Davey, and D. Anderson, 1995: Decadal and seasonal dependence of ENSO prediction skill. *J. Climate*, **8**, 2705–2715.

Barnston, A., H. van den Dool, S. Zebiak, T. Barnett, M. Ji, D. Rodenhuis, M. Cane, A. Leetmaa, N. Graham, C. Ropelewski, V. Kousky, E. O'Lenic, and R. Livezey, 1994: Long-lead seasonal forecasts - where do we stand? *Bull. American Met. Soc.*, **75**, 2097–2114.

Bottomley, M., C. K. Folland, J. Hsiung, R. E. Newell, and D. E. Parker, 1990: *Global Ocean Surface Temperature Atlas.* HMSO. Publication funded by UK depts of Energy and Environment.

Chang, P., L. Ji, and H. Li, 1997: A decadal climate variation in the tropical Atlantic Ocean from thermodynamic air-sea interactions. *Nature*, **385**, 516–518.

Cox, M. D., 1984: A primitive equation, three dimensional model of the ocean. GFDL Ocean Group Technical Report 1, GFDL.

Cullen, M. J. P., 1993: The Unified forecast/climate model. *Met. Magazine*, **122**, 81–94.

Davey, M. K., S. Ineson, and M. A. Balmaseda, 1994: Simulation and hindcasts of tropical Pacific Ocean interannual variability. *Tellus*, 433–477.

Delworth, T., 1996: North atlantic interannual variability in a coupled ocean-atmosphere model. *J. Climate*, **9**, 2356–2375.

Diaz, H., and V. Markgraf, 1992: *El Niño. Historical and paleoclimatic aspects of the Southern Oscillation.* Cambridge University Press. 471pp.

Dolman, A. J., and D. Gregory, 1992: The parametrization of rainfall interception in GCMs. *Quart. Journ. R. Met. Soc.*, **118**. 455–468.

Glantz, M. H., R. W. Katz, and N. Nicholls, Eds., 1991: *Teleconnections linking Worldwide Climate anomalies.* Cambridge University Press. 535pp.

Gregory, D., and P. R. Rowntree, 1990: A mass flux convection scheme with representation of cloud ensemble characteristics and stability-dependent closure. *Monthly Weather Review*, **118**(7), 1483–1506.

——, and R. N. B. Smith, 1990: Canopy, surface and soil hydrology. Unified Model documentation paper 25, Meteorological Office, London Rd, Bracknell, Berkshire. RG12 2SY.

Gu, D., and S. Philander, 1995: Secular changes of annual and interannual variability in the tropics during the last century. *J. Climate*, **8**, 864–876.

——, and ——, 1997: Interdecadal climate fluctuations that depend on exchanges between the tropics and the extratropics. *Science*, **275**, 805–807.

Harrisson, E. F., P. Minnis, B. R. Barkstrom, V. Ramanathan, R. D. Cess, and G. G. Gibson, 1990: Seasonal variation of cloud radiative forcing derived from the Earth radiation budget experiment. *J. Geophys. Res.*, **95**(D11), 18687–18703.

Hewitt, C. D., and J. F. B. Mitchell, 1996: GCM simulations of the climate of 6k B.P. : mean changes and inter-decadal variability. *J. Clim.*, **9**, 3505–3529.

Ineson, S., and M. Davey, 1997: Interannual climate simulation and predictability in a coupled TOGA GCM. *Mon. Wea. Rev (to appear).*

Ji, M., and T. Smith, 1995: Ocean model response to temperature data assimilation and varying surface wind stress: intercomparisons and implications for climate forecast. *Mon.Wea.Rev.*, **123**, 1811–1821.

——, A. Leetmaa, and J. Derber, 1995: An ocean analysis system for seasonal to interannual climate studies. *Mon. Wea. Rev.*, **123**, 460–481.

Johns, T. C., R. E. Carnell, J. F. Crossley, J. M. Gregory, J. F. B. Mitchell, C. A. Senior, S. F. B. Tett, and R. A. Wood, 1997. The second Hadley Centre coupled ocean-atmosphere GCM: Model description, spinup and validation. Accepted by *Cli. Dyn.*

Kraus, E. B., and J. S. Turner, 1967: A one dimensional model of the seasonal thermocline. Part II. *Telus*, **19**, 98–105.

Kushnir, Y., 1994: Interdecadal variations in North Atlantic sea surface temperature and associated atmospheric conditions. *J. Climate*, **7**, 141–157.

Latif, M., and T. P. Barnett, 1994: Causes of decadal climate variability over the North Pacific and North America. *Science*, **226**, 634–637.

——, and T. Barnett, 1996: Decadal variability over the North Pacific and North America: dynamics and predictability. *J. Climate*, **9**, 2407–2423.

——, A. Sterl, E. Maier-Reimer, and M. M. Junge, 1993a: Climate variability in a coupled GCM. Part I: The tropical Pacific. *J. Climate*, **6**, 5–21.

——, ——, ——, and M. Junge, 1993b: Structure and predictability of the El Niño/Southern Oscillation phenomenon in a coupled ocean-atmosphere general circulation model. *J.Clim.*, **6**, 700–708.

——, 1996: Dynamics of interdecadal variability in coupled ocean-atmosphere models. white paper Oct, CLIVAR workshop, Villefranche.

Lau, N.-C., S. G. H. Philander, and M. J. Nath, 1992: Simulation of ENSO-like phenomena with a low-resolution coupled GCM of the global ocean and atmosphere. *J. Climate*, **5**, 284–307.

Leetmaa, A., and M. Ji, 1989: Operational hindcasting of the tropical Pacific. *Dynamics of Atmospheres and Oceans*, **13**, 465–490.

Levitus, S., 1982: Climatological atlas of the world ocean. Professional Paper 13, National Oceanic and Atmospheric Administration, Rockville, Maryland.

Manabe, S., R. J. Stouffer, M. J. Spelman, and K. Bryan, 1991: Transient responses of a coupled ocean-atmosphere model to gradual changes of atmospheric CO_2. Part I: Annual mean response. *J. Climate*, **4**(8), 785–818.

Mann, M., and J. Park, 1994: Global-scale modes of surface temperature variability on interannual to century timescales. *J. Geophys. Res.*, **99**, 25819–25833.

Mechoso, C., A. Robertson, N. Barth, M. Davey, P. Delecluse, P. Gent, S. Ineson, B. Kirtman, M. Latif, H. L. Treut, T. Nagai, J. Neelin, S. Philander, J. Polcher, P. Schopf, T. Stockdale, M. Suarez, L. Terray, O. Thual, and J. Tribbia, 1995: The seasonal cycle over the tropical pacific in coupled ocean-atmosphere general circulation models. *Mon. Wea. Rev.*, **123**, 2825–2838.

Meehl, G. A., M. Wheeler, and W. M. Washington, 1994: Low-frequency variability and CO_2 transient climate change. part 3. Intermonthly and interannual variability. *Climate Dynamics*, **10**, 277–303.

——, 1987: The annual cycle and interannual variability in the tropical Pacific and Indian ocean regions. *Monthly Weather Review*, **115**, 27–50.

——, 1990: Seasonal cycle forcing of El-Niño-Southern Oscillation in a global, coupled ocean-atmosphere GCM. *J. Climate*, **3**, 72–98.

——, 1993: A coupled air-sea biennial mechanism in the tropical Indian and Pacific regions: Role of the ocean. *J. Climate*, **6**(1), 31–41.

Mitchell, J. F. B., T. C. Johns, J. M. Gregory, and S. F. B. Tett, 1995: Climate response to increasing levels of greenhouse gases and sulphate aerosols. *Nature*, **376**, 501–504.

Murphy, J. M., and J. F. B. Mitchell, 1995: Transient response of the Hadley Centre coupled ocean-atmosphere model to increasing carbon dioxide. Part II: Spatial and temporal structure of response. *J. Clim.*, **8**, 57–80.

Nagai, T., T. Tokioka, M. Endih, and Y. Kitamura, 1992: El Niño-Southern Oscillation simulated in an MRI atmosphere-ocean coupled general circulation model. *J. Climate*, **5**, 1202–1233.

Neelin, J. D., M. Latif, M. A. F. Allart, M. A. Cane, U. Cubasch, W. L. Gates, P. R. Gent, C. Gordon, C. R. Mechoso, G. A. Meehl, J. M. Oberhuber, S. G. H. Philkander, P. S. Schopf, K. R. Sperber, A. Sterl, T. Tokioka, J. Tribbia, and S. E. Zebiak, 1992: Tropical air-sea interaction in general circulation models. *Climate Dynamics*, **7**, 73–104.

Pacanowski, R. C., and S. G. Philander, 1981: Parameterization of vertical mixing in numerical models of tropical oceans. *J. Phys. Oceanogr.*, **11**, 1443–1451.

Parker, D., C. K. Folland, M. N. Ward, A. Bevan, M. Jackson, and K. Maskell, 1993: Marine surface data for analysis of climate fluctuations on interannual to century timescales. *Proc. National Academy of Science National Research council workshop on climate variability on Decade to Centuary time scales, Irvine, Cal., USA, 21-25 Sept 1992.*

Parker, D. E., P. D. Jones, C. K. Folland, and A. Bevan, 1994: Interdecadal changes of surface temperature since the late nineteenth century. *J. Geophys. Res*, **99**, 14373–14399.

——, 1983: Documentation of a Southern Oscillation index. *Meteorological Magazine*, **112**, 184–187.

Philander, S. G. H., N. C. Lau, R. C. Pacanowski, and M. J. Nath, 1989: Two different simulations of the Southern Oscillation and El-Niño with coupled ocean-atmosphere general circulation models. *Phil. Trans. R. Soc. Lond. A*, **329**, 167–178.

——, R. C. Pacanowski, N.-C. Lau, and M. J. Nath, 1992: Simulation of ENSO with a global atmosphere GCM coupled to a high-resolution tropical Pacific ocean GCM. *J. Climate*, **5**, 308–329.

Philander, S. G., 1990: *El Niño, La Niña, and the Southern Oscillation*, volume 46 of *International Geophysics Series*. Academic Press.

Rasmusson, E. M., and T. H. Carpenter, 1982: Variations in tropical sea surface temperature and surface wind fields associated with the Southern Oscillation/El-Niño. *Monthly Weather Review*, **110**, 354–384.

Rasmusson, E., X. Wang, and C. Ropelewski, 1990: The biennial component of ENSO variability. *Journal of Marine Systems*, **1**, 71–96.

Robertson, A., C.-C. Ma, M. Ghil, and C. Mechoso, 1995: Simulation of the tropical Pacific climate with a coupled ocean-atmosphere general circulation model. Part II: Interannual variabilty. *J. Clim.*, **8**, 1199–1216.

Ropelewski, C., and P. Jones, 1987: An extension of the Tahiti-Darwin Southern Oscillation index. *Mon. Wea. Rev.*, **115**, 2161–2165.

Santer, B., K. Taylor. T. Wigley, T. Johns, P. Jones, D. Karoly, J. Mitchell, A. Oort, J. Penner, V. Ramaswamy, M. Schwarzkopf, R. Stouffer, and S. Tett, 1996: A search for human influences on the thermal structure of the atmosphere. *Nature*, **382**, 39–45.

Slingo, A., 1989: A GCM parametrization for the shortwave radiative properties for clouds. *J.Atmos.Sci*, **46**, 1419–1427.

Smith, T., and M. Chelliah, 1995: The annual cycle in the tropical pacific ocean based on assimilated ocean data from 1983 to 1992. *J. Climate*, **8**, 1600–1614.

Smith, R. N. B., 1990: A scheme for predicting layer clouds and their water content in a general circulation model. *Quart. J. R. Met. Soc.*, **116**, 435–460.

Sperber, K. R., and S. Hameed, 1991: Southern Oscillation simulation in the OSU coupled upper ocean-atmosphere GCM. *Climate Dynamics*, **6**, 83–97.

Terray, L., O. Thual, S. Belamari, M. Deque, P. Dandin, C. Levy, and P. Delecluse, 1995: Climatology and interannual variability simulated by the ARPEGE-OPA model. *Clim. Dyn.*, **11**, 487–505.

Tett, S. F. B., J. F. Mitchell, D. E. Parker, and M. R. Allen, 1996: Human influence on the atmospheric vertical temperature structure: Detection and observations. *Science*, **247**, 1170–1173.

——, T. C. Johns, and J. Mitchell, 1997. Global and regional variability in a coupled AOGCM. Accepted by *Cli. Dyn.*

Tett, S., 1995: Simulation of El-Niño/Southern Oscillation like variability in a global AOGCM and its response to CO_2 increase. *J. Clim.*, **8**(6), 1473–1502.

TOGA, 1997: Special review volume. *J. Geophys. Res., Oceans (To appear).*

Wang, X., and C. Ropelewski, 1995: An assessment of ENSO-scale secular variability. *J. Climate*, **8**, 1584–1599.

Wang, B., 1995: Interdecadal changes in El-Niño onset in the last four decades. *J. Climate*, **8**, 267–285.

Washington, W. M., and G. M. Meehl, 1989: Climate sensitivity due to increased CO_2: Experiments with a coupled atmosphere and ocean general circulation model. *Climate Dynamics*, **4**, 1–38.

Woodruff, S., R. Slutz, R. Jenne, and P. Steurer, 1987: A comprehensive ocean-atmosphere data set. *Bull. Am. Met. Soc.*, **68**, 1239–1250.

Zebiak, S. E., and M. A. Cane, 1987: A model El Niño–Southern Oscillation. *Monthly Weather Review*, **115**(10), 2262–2278.

Zhang, C., 1993: Large-scale variability of atmospheric deep convection in relation to sea surface temperature in the tropics. *J. Climate*, **6**(10), 1898–1913.

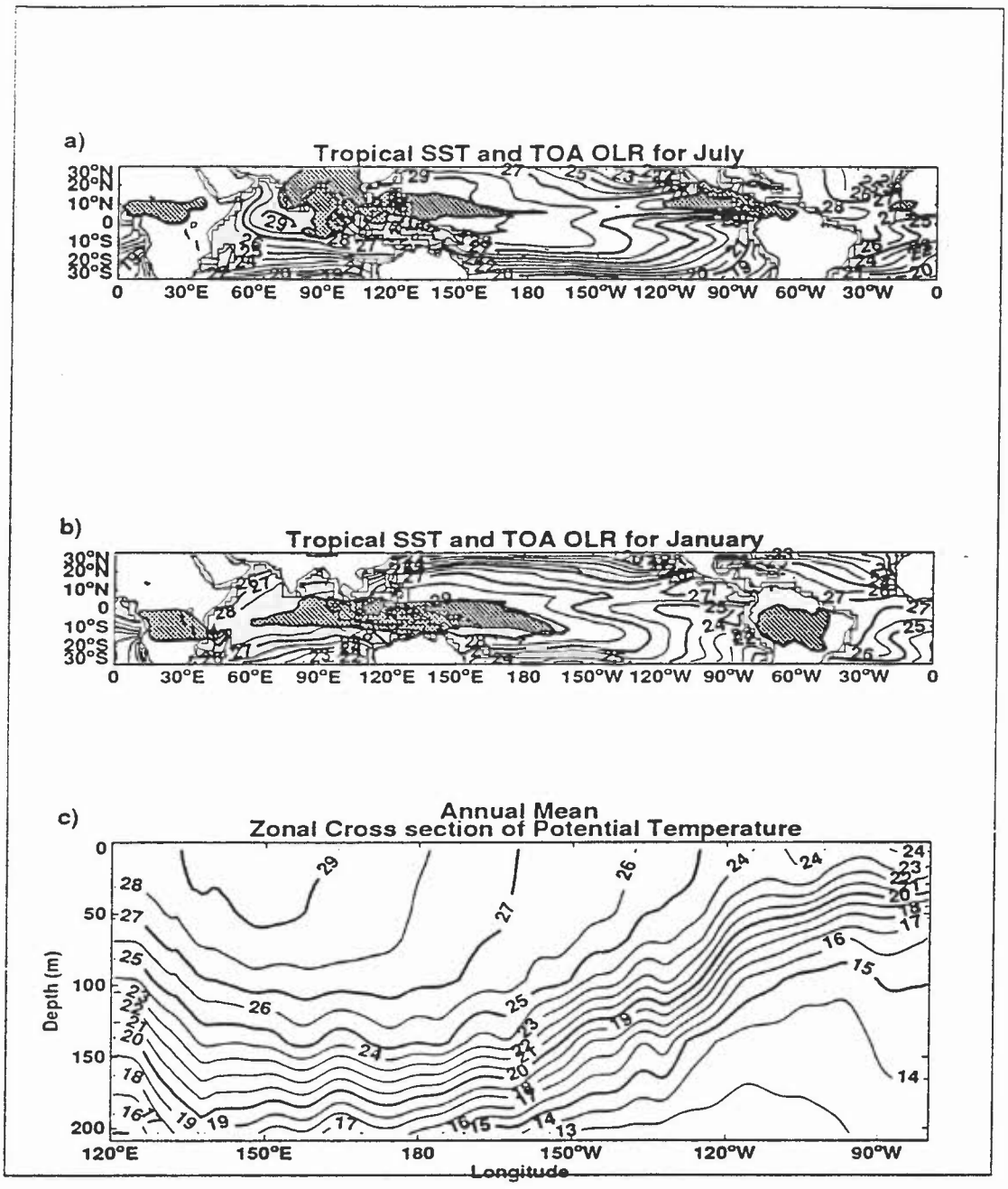

Figure 1: Observed tropical climatology

Plots (a) and (b) show the observed sea surface temperature in the tropics for July and January respectively using GISST data for 1985–89 for which period ERBE data is available Plot (c) shows an equatorial section of annual mean ocean temperature in the Pacific (averaged from 2.5N to 2.5S) using Levitus (1982) data.

A contour interval of 1°C is used in all plots. Below 26°C every 5th contour is bold, above 26°C every odd contour is bold.

Also shown in plots (a) and (b) by stippling are regions where the outgoing longwave radiation at the top of the atmosphere is less than 220W/m^2 taken from ERBE data.

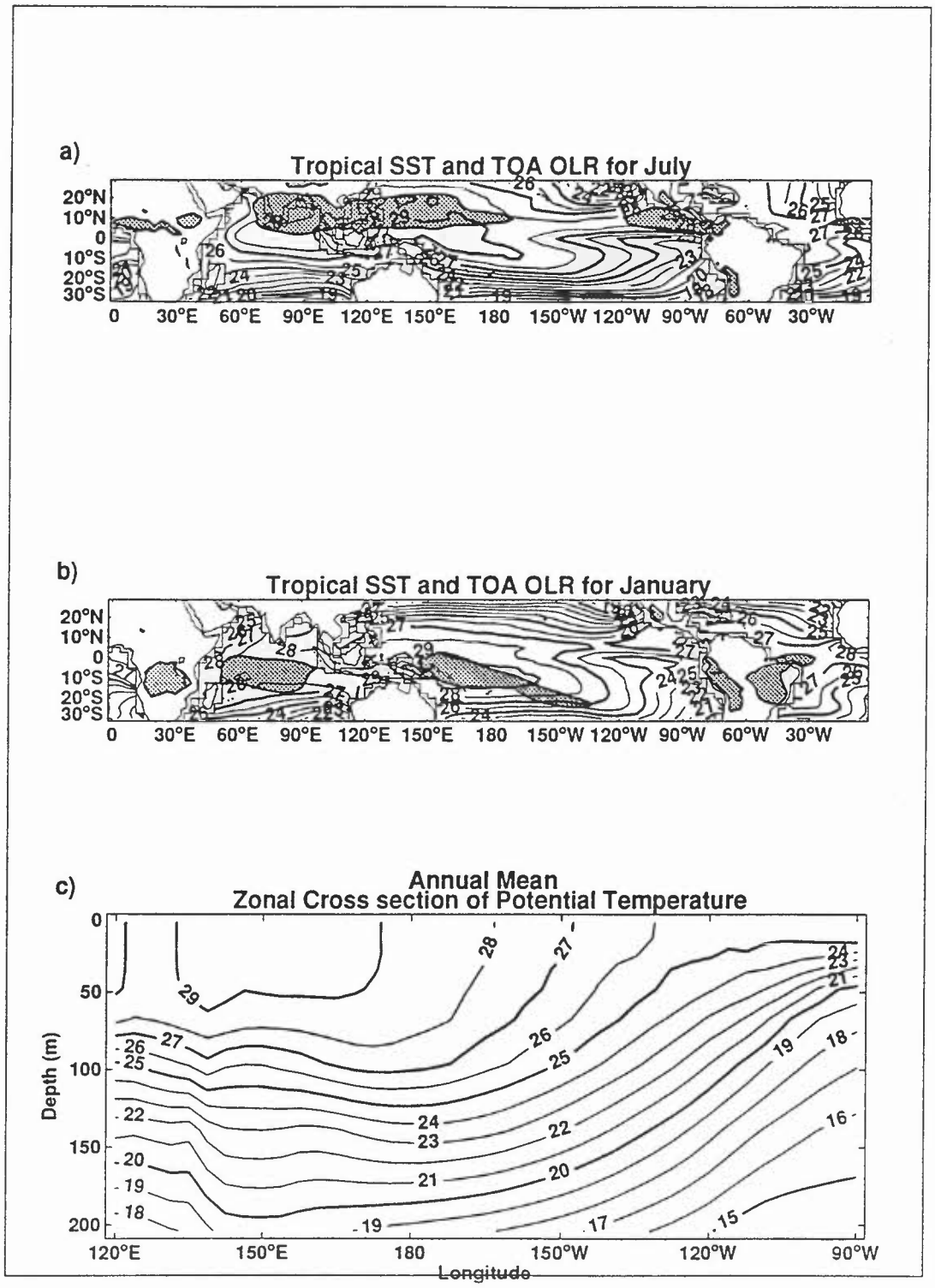

Figure 2: HADCM tropical climatology

The plots, contours and shading are the same as in Fig. 1 except that they are taken from the HADCM experiment.

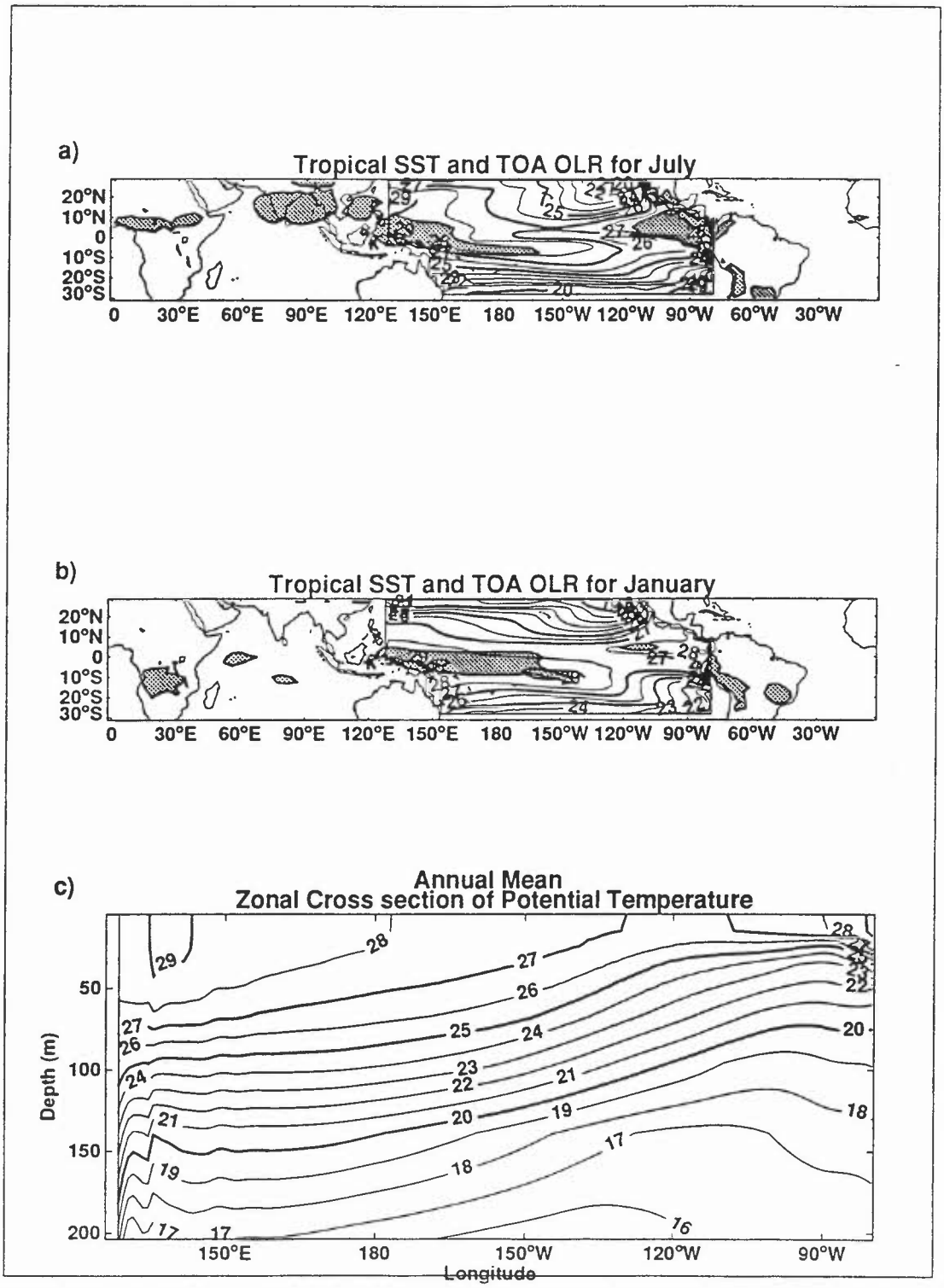

Figure 3: TOGAGCM tropical climatology

The plots, contours and shading are the same as in Fig. 1 except that they are taken from the TOGAGCM simulation.

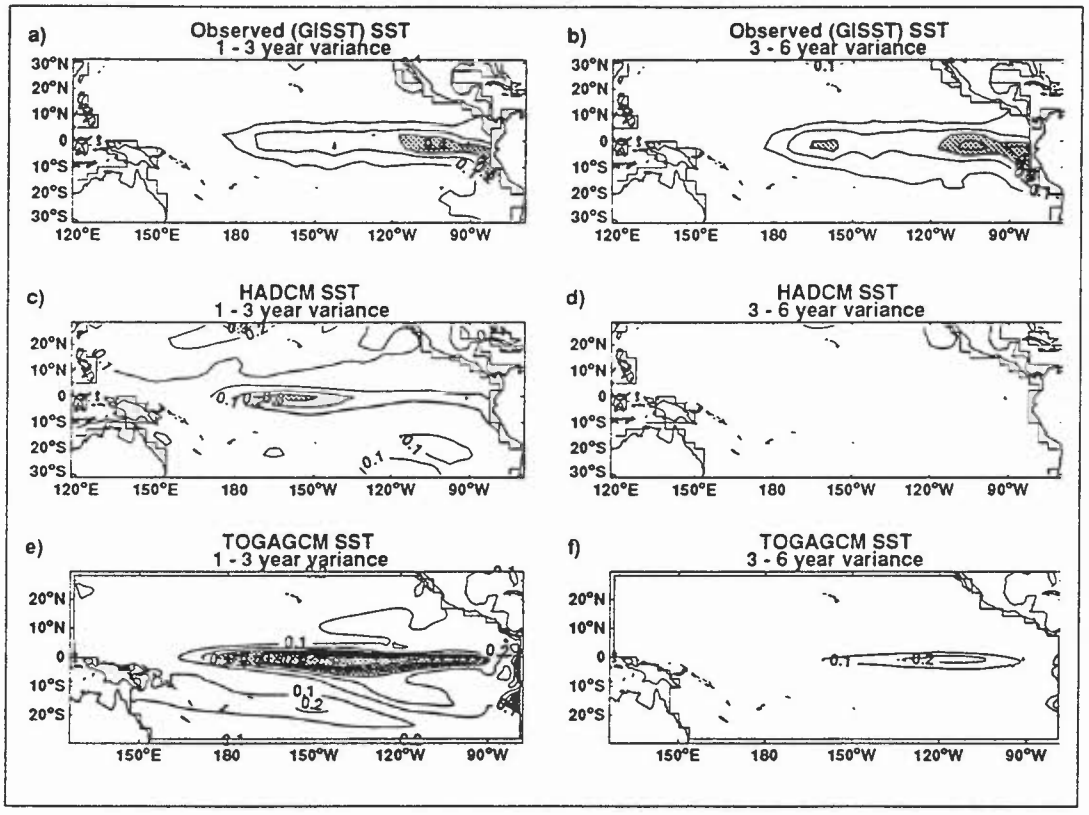

Figure 4: SST filtered variance

Panels (a), (c), and (e) show the total power in the 1+ to 3 year period range for observations, the HADCM and the TOGAGCM models respectively. Panels (b), (d), and (f) show the corresponding total power in the 3+ to 6 year period range. A contour interval of $0.1K^2$ is used in all plots with shading for values above $0.3K^2$.

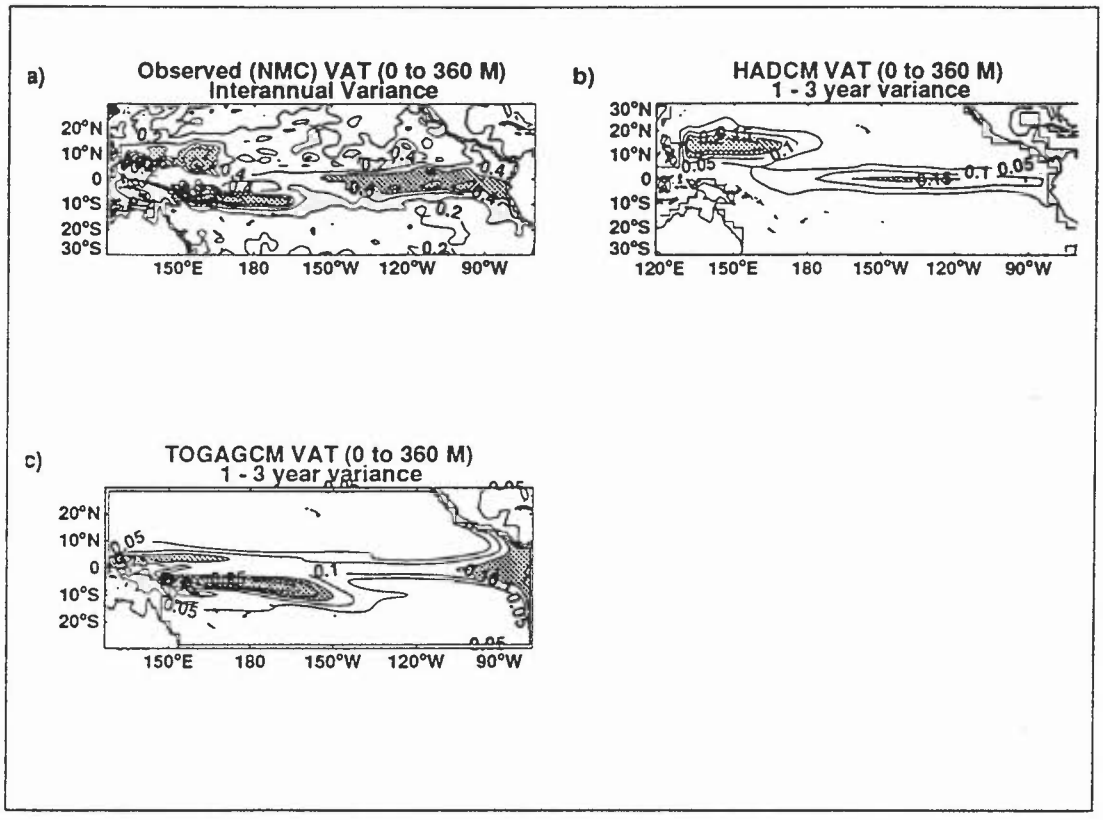

Figure 5: VAT filtered interannual variance

Filtered variance of vertically averaged temperature (VAT) from the surface to a depth of 360 metres is shown. Panel (a) is from 11 years of NMC RA3 analysis data. A contour interval of $0.2K^2$ is used, with stippling where values are greater than $0.6K^2$. Panels (b) and (c) contain similar plots for the HADCM and TOGAGCM models, but with a contour interval of 0.05 K^2 and stippling for values greater than 0.15 K^2.

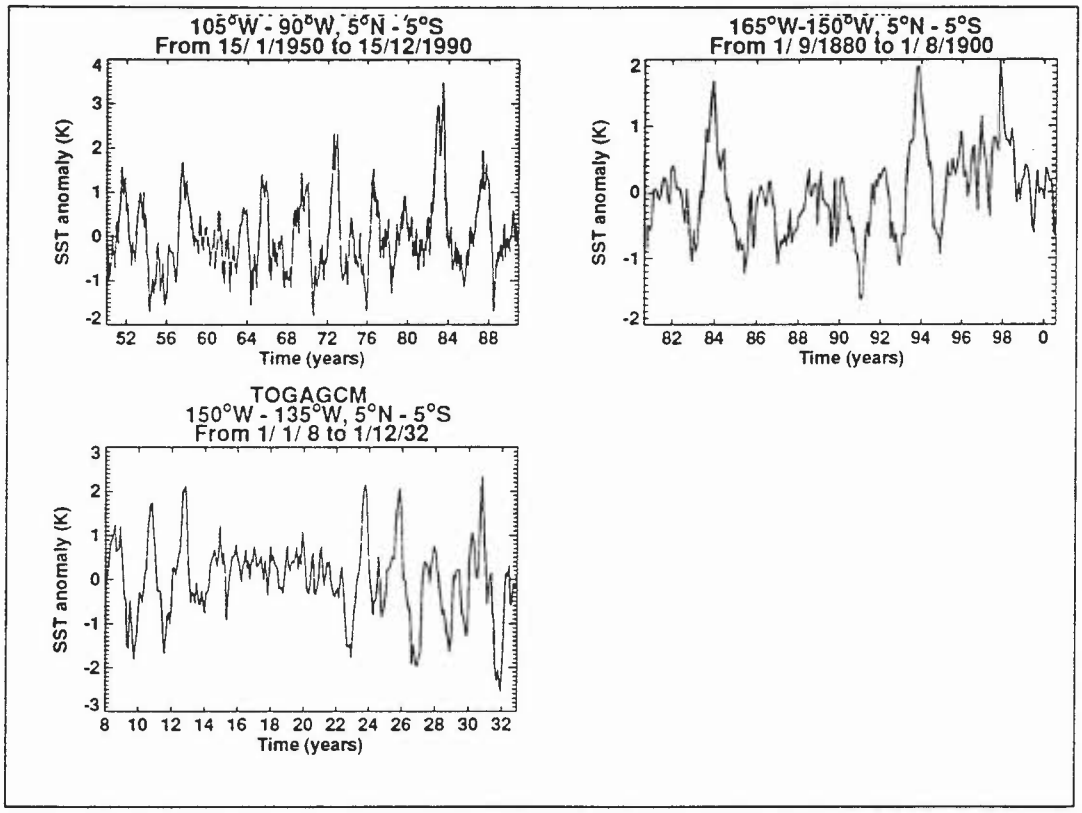

Figure 6: Observed and model SST timeseries

Plot (a) shows 40 years of observed SST anomalies, plot (b) shows SST anomalies from the 20 year HADCM simulation, and plot (c) shows SST anomalies from the 25 year TOGAGCM simulation.

The anomalies were calculated in the regions of maximum inter-annual variance: 105°W to 90°W for the observations, 165°W to 150°W for HADCM, 150°W to 135°W for TOGAGCM. Each region extends from 5°N to 5°S.

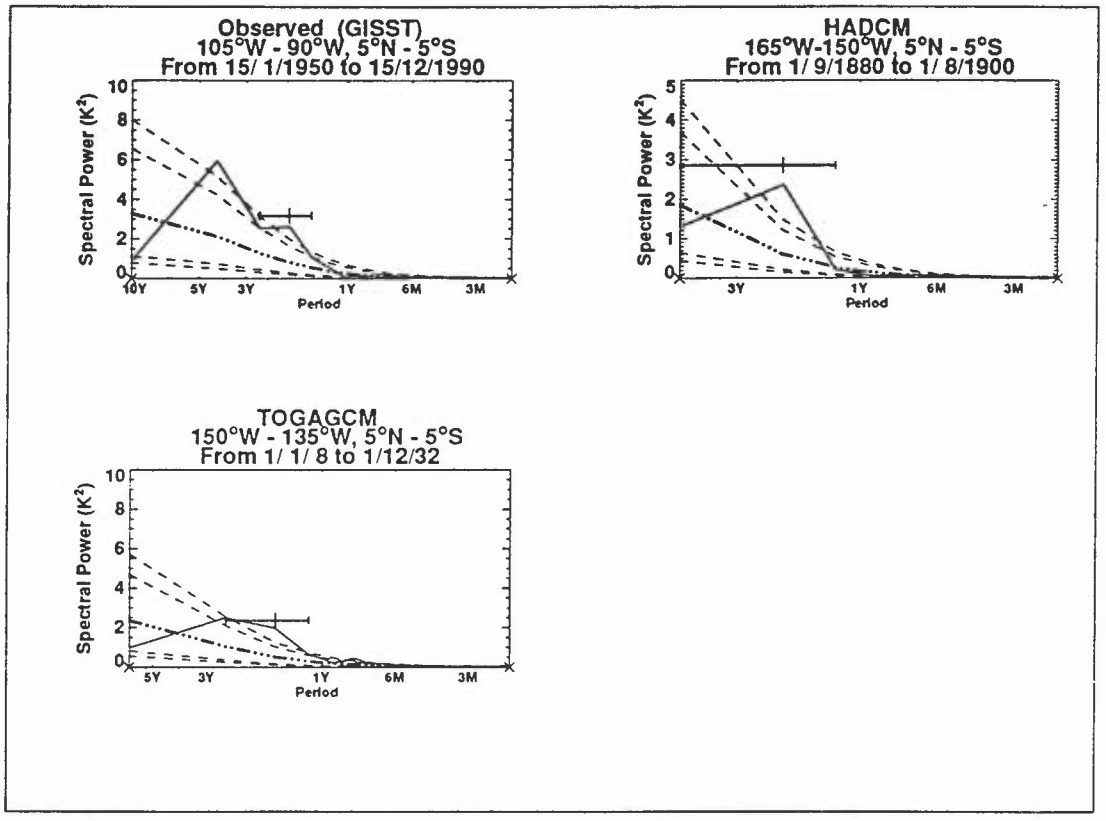

Figure 7: Observed and Modelled SST power spectra
Power spectra of SST for the same maximum variance regions used in Fig. 6. The thick dot-dashed lines indicate a best-fit red noise power spectrum. The dashed lines show the 95% and 99% confidence limits – lines closer to the red noise spectrum correspond to smaller confidence limits. The bandwidth is shown by the error bar centred near the region of maximum power. The height of each ordinate is the estimated power in each frequency range multiplied by the total number of frequencies.

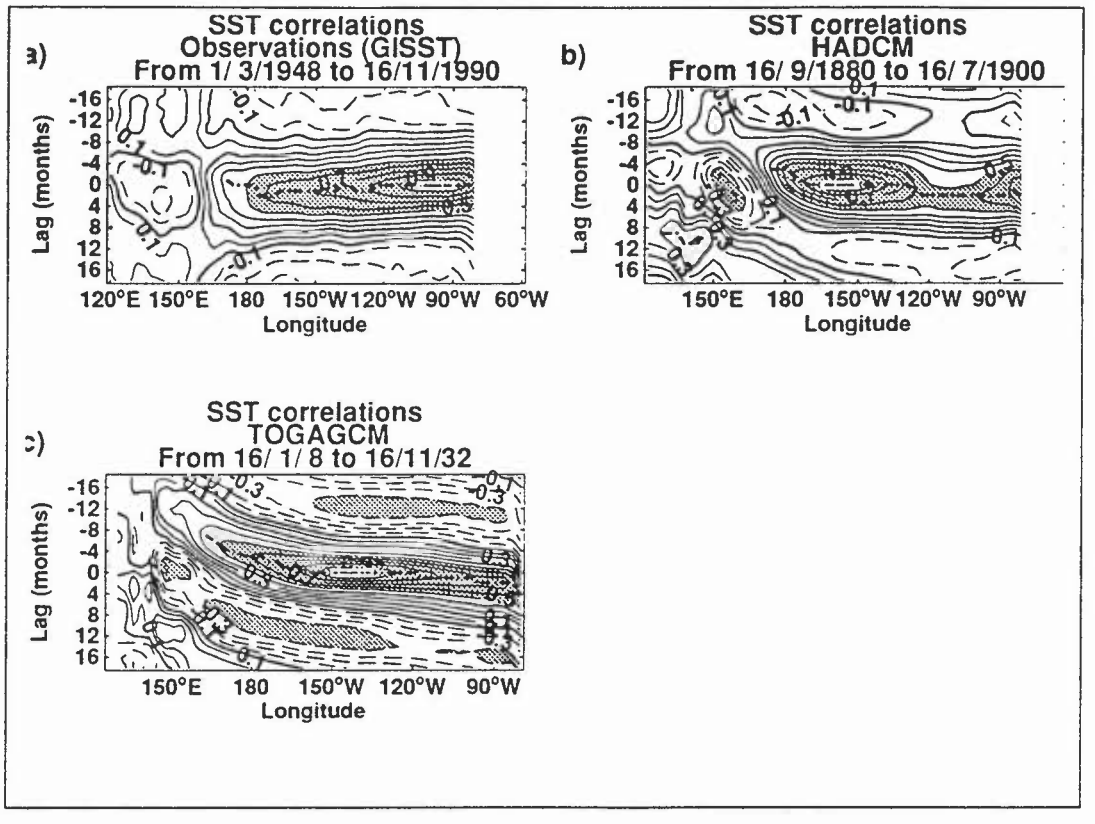

Figure 8: SST/SST correlations

Lag correlations between SST anomalies (averaged from 5°N to 5°S) across the equatorial Pacific and the region of maximum interannual SST variability (shown by a box in each plot) for (a) observations, (b) HADCM, and (c) TOGAGCM.

The contour interval is 0.1 and stippling is used where correlations are less than −0.6 or greater than 0.6. Negative contours are drawn dashed, every odd contour is labeled, and every even contour is bold. The thick dot-dashed line joins the positions of the maximum correlations, where the maximum is greater than 0.4.

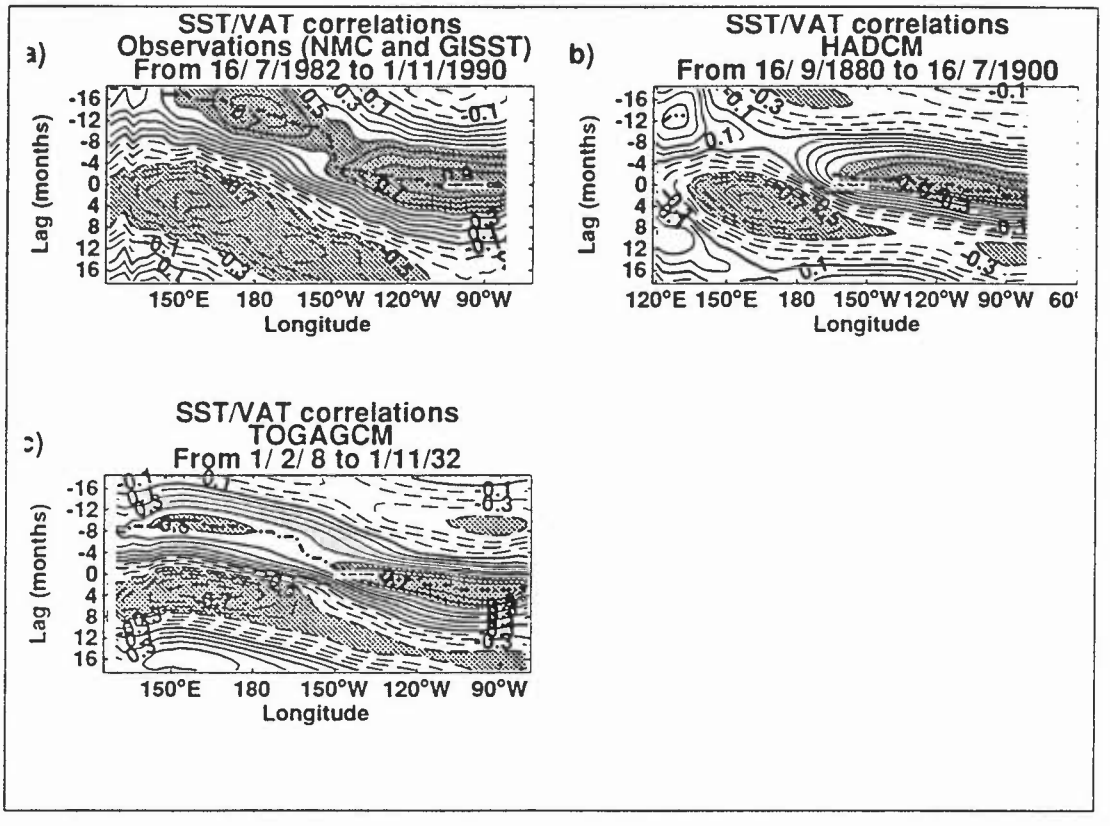

Figure 9: SST/VAT correlations

Lag correlations between VAT anomalies (averaged from 5°N to 5°S) across the equatorial Pacific and the region of maximum interannual SST variability (shown by a box in each plot) for (a) observations, (b) HADCM, and (c) TOGAGCM.

The contour interval is 0.1 and stippling is used where correlations are less than −0.6 or greater than 0.6. Negative contours are drawn dashed, every odd contour is labeled, and every even contour is bold. The thick dot-dashed line joins the positions of the maximum correlations, where the maximum is greater than 0.4.

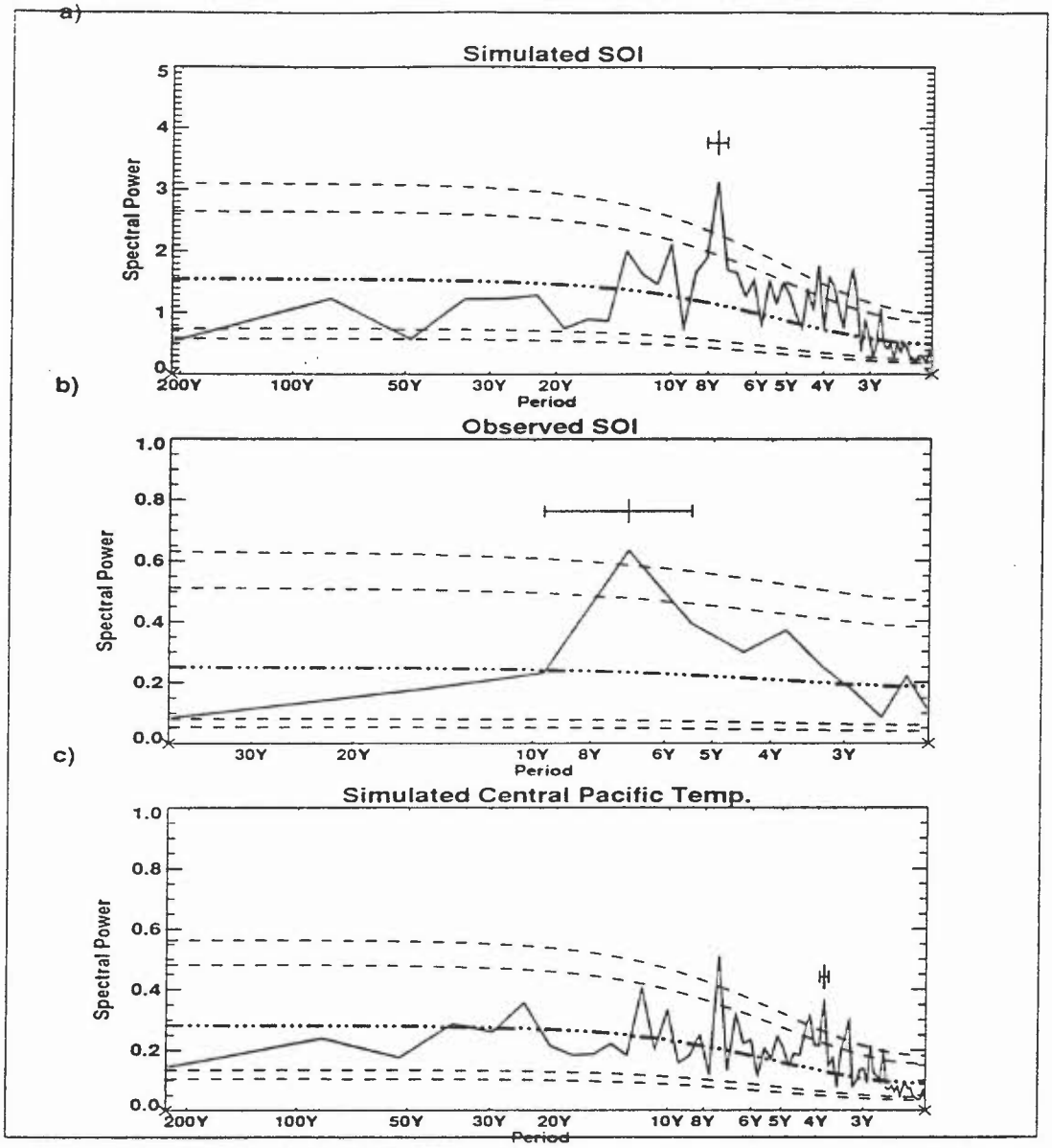

Figure 10: Power spectra for simulated and observed SOI

Plot (a): SOI from 1300 years of HADCM2 simulation. The model SOI is the pressure difference between "Darwin" (area average for the region 125°W, 15°S - 130°W, 10°S) and "Tahiti" (area average for the region 150°E, 20°S - 155°E, 15°S). The spectrum has been averaged in groups of 10 frequency bins.

Plot (b): as (a) except for observed SOI and averaging in groups of 5 frequency bins. Annual mean data are used.

Plot (c): simulated SST from HADCM2 in the central Pacific region (180° - 150°W, 5°S - 5°N).

The thick dot-dashed lines in each panel indicate a best-fit red noise power spectrum. The dashed lines show the 95% and 99% confidence limits - lines closer to the red noise spectrum correspond to smaller confidence limits. The bandwidth is shown by the error bar centred near the region of maximum power.